crystals

MDPI

Article

A Theoretical Investigation of the Structural and Electronic Properties of P/$SnBr_2$ Heterojunctions

Kun Yang [1], Zongling Ding [2,*], Qi Hu [1], Jin Sun [2,*] and Qiuju Li [2]

[1] School of Materials Science and Engineering, Anhui University, Hefei 230601, China
[2] School of Physics and Optoelectronics Engineering, Anhui University, Hefei 230601, China
* Correspondence: zlding@ahu.edu.cn (Z.D.); sunjin@ahu.edu.cn (J.S.)

Abstract: In this paper, the structural and electronic properties of P/$SnBr_2$ heterojunctions were investigated using the first-principles calculation method based on the density functional theory (DFT). The band alignment of the P/$SnBr_2$ heterojunction was type I. The bandgap value was 0.71 eV in the DFT calculation. Furthermore, the bandgap of the heterojunction could be efficiently tuned by controlling an electric field and biaxial strain. The bandgap changed linearly with the electric field in a certain range; when the electric field was greater than 0.8 V/Å, the heterojunction was metallic. The bandgap could also be tuned when a biaxial strain was applied. Under tensile or compressive stress, significant effects such as the band alignment shift from type I to type III, and the transition from indirect to direct bandgap occurred. In conclusion, these research findings provide theoretical guidance for designing new heterojunctions based on $SnBr_2$.

Keywords: two-dimensional heterostructure; electric field; biaxial strain; bandgap; density functional theory

Citation: Yang, K.; Ding, Z.; Hu, Q.; Sun, J.; Li, Q. A Theoretical Investigation of the Structural and Electronic Properties of P/$SnBr_2$ Heterojunctions. *Crystals* **2023**, *13*, 1077. https://doi.org/10.3390/cryst13071077

Academic Editor: Andreas Thissen

Received: 14 June 2023
Revised: 6 July 2023
Accepted: 6 July 2023
Published: 8 July 2023

1. Introduction

The discovery of graphene has led to extensive research on the physical and chemical properties of two-dimensional (2D) materials [1,2]. Nowadays, various kinds of 2D materials, such as the transition metal dichalcogenides (TMDCs) [3,4], hexagonal boron nitride (h-BN) [5] and phosphorylenes [6–8], are common platforms used in optoelectronic and electronic applications due to their unique material properties [9,10], and have attracted much attention. Due to their valuable optical, electronic, chemical, magnetic and mechanical properties, which are significantly different from the conventional bulk materials, 2D materials show great potential for the development of various nanodevices [11,12].

Unlike most multilayer TMDCs with indirect bandgaps, phosphorene of different thicknesses always have a direct bandgap, which is a significant advantage for optoelectronic applications. Moreover, the carrier mobility of phosphorene is notably greater than that of other 2D materials, such as the transition metal dichalcogenides (TMDCs) [13,14]. When the thickness of phosphorene is about 10 nm, the ground carrier mobility of black phosphorus can reach 1000 $cm^2 \cdot V^{-1} \cdot s^{-1}$ [15]. Compared with graphene, phosphorene can conduct electrons at a rate similar to graphene, and has a considerable bandgap, which makes it significantly better than graphene with zero bandgap. The outstanding feature of layered phosphorene is its in-plane anisotropy, which results in an angle-dependent optical conductivity and carrier mobility [16,17]. Due to its unique structure, excellent physical properties and anisotropy, phosphorene has great potential in field-effect transistors (FETs), photodetectors, batteries, thermoelectric applications and other fields [18–20], while it is rare in other 2D materials. The monolayer structure of phosphorene is the second basic monolayer material after graphene, which can be exfoliated from the bulk crystal to produce unique properties. Tin halide compounds and related materials are being explored as promising lead-free hybrid materials. There has been significant progress in developing

organic tin halide compounds with varying structures and controllable dimensions on a molecular level. Recently, lead-free metal halide perovskite and hybrid power mines have attracted more and more interest in various optoelectronic applications, from solar cells to light-emitting diodes and sensors [21,22].

In recent years, the discovery of more and more 2D materials has triggered the explosive expansion in the study of van der Waals (vdW) heterostructures [23–25]. Due to suspension-free bonding surfaces and weak vdW interlayer interactions, different 2D materials can be stacked vertically to form different heterostructures. These heterostructures are not limited to the properties of a single 2D material, and can combine the advantages of the individual components to achieve different functions [26,27]. By forming heterostructures, one can not only break the limitations of monolayer materials, but also the new structures of multilayer materials often show excellent optoelectronic properties, which expands the application of this material in the new generation of optoelectronic nanodevices. For example, a heterostructure with the vertical stacking of $MoSe_2/PtSe_2$ was synthesized by Zhou et al. The direct bandgap structure with type-II energy band arrangement between $PtSe_2$ and $MoSe_2$ was confirmed by first-nature principle calculations [28]. He et al. synthesized $In_2SeS/g\text{-}C_3N_4$ and could effectively tune the energy band structure of the system by controlling the stacking pattern of the 2D heterojunction, thus, obtaining various electronic properties [29]. Zhang et al. demonstrated that the $MoSe_2/WSe_2$ heterostructure is a type-II vdW using the application of an electric field [30]. So far, there have been many studies based on 2D heterojunctions. However, the problems related to the bandgap in 2D materials are still a hot topic of research. For example, the zero-bandgap property of graphene limits its application in electronic and optoelectronic devices [31]. h-BN has a large bandgap and is an insulator [32]. Researchers have been searching for new 2D materials with moderate bandgaps that are highly advantageous for fabricating electronic and optoelectronic devices, and the tuning of their electronic structure and properties is of great importance. Phosphole is considered as a promising candidate for new electronic devices due to its direct energy gap and high carrier mobility at room temperature [33]. At the same time, low-dimensional tin halide compounds are more stable than 3D tin halide perovskite, because organic cations have better protection for photo active tin halides [34,35].

Considering the significant characteristics of the 2D tin bromide and phosphorene monolayer, we suggested creating a novel heterojunction of $P/SnBr_2$ to enhance their benefits in optoelectronic and solar devices. In this paper, the structure and electronic properties of $P/SnBr_2$ heterojunctions were mainly discussed using the first principle method based on DFT. The results showed that the heterojunction had an atypical type I band arrangement. The calculation results showed that the bandgap of $P/SnBr_2$ heterojunction was -0.08~0.83 eV under the applied electric field. The bandgap varied from -0.015 to 1.04 eV when a biaxial strain was applied, which can be applied to solar energy and photoelectric devices. This suggested that the new heterojunction could be applied to solar devices and optoelectronic devices.

2. The Computational Details

In order to systematically study the electronic properties of $P/SnBr_2$, the first principle method based on the density functional theory (DFT) was adopted in this paper, and the properties of the heterojunction were calculated by the Vienna Ab-initio Simulation Package (VASP) [36,37]. The exchange correlation potential was described by Predew Bourke Ernzerhof (PBE) under the generalized gradient approximation (GGA), which has been proven to be suitable for 2D material heterojunction systems [38–40]. The conjugate gradient method was used to optimize the atomic positions and lattice parameters. The convergence criterion of the total energy was set to 10^{-5} eV, the force convergence criterion for individual atoms was 0.01 eV/Å, and the plane-wave cutoff energy was set to 500 eV. The Brillouin zone was sampled as a whole using a $3 \times 11 \times 1$ grid centered on the gamma point [41], taking into account the effect of the interlayer vdW forces; the DFT-2 was used for correction. The impact of spin–orbit coupling on the heavy atoms was considered

throughout the entire calculation process. In the construction of the heterojunction model, a vacuum layer of 20 Å was added along the Z-axis to avoid the influence of periodicity on the structure.

3. Results and Discussion

3.1. The Atomic Structure of P/$SnBr_2$ Heterojunctions

Prior to computing the pertinent characteristics of the heterojunction, we conducted a structural optimization of both the phosphorene and $SnBr_2$ monolayers. After the structural optimization, the lattice parameters of phosphorene were a = 3.30 Å and b = 4.60 Å [42]. The initial configuration of $SnBr_2$ was 1T-phase $SnBr_2$ (space group P3m1) with structurally optimized lattice parameters a = 4.26 Å and b = 4.36 Å. In order to reduce the lattice mismatch during the construction of the heterojunction, we expanded the phosphorene into a 5 × 1 supercell and transformed the initial configuration of $SnBr_2$ from a hexagonal unit into a tetragonal unit, and then expanded it into a 2 × 1 supercell. The lattice mismatch ratio of the heterojunction formed by two monolayers was 5.2%. The lattice parameters of the heterojunction were a = 15.87 Å and b = 4.50 Å. The structure of the heterojunction is shown in Figure 1a.

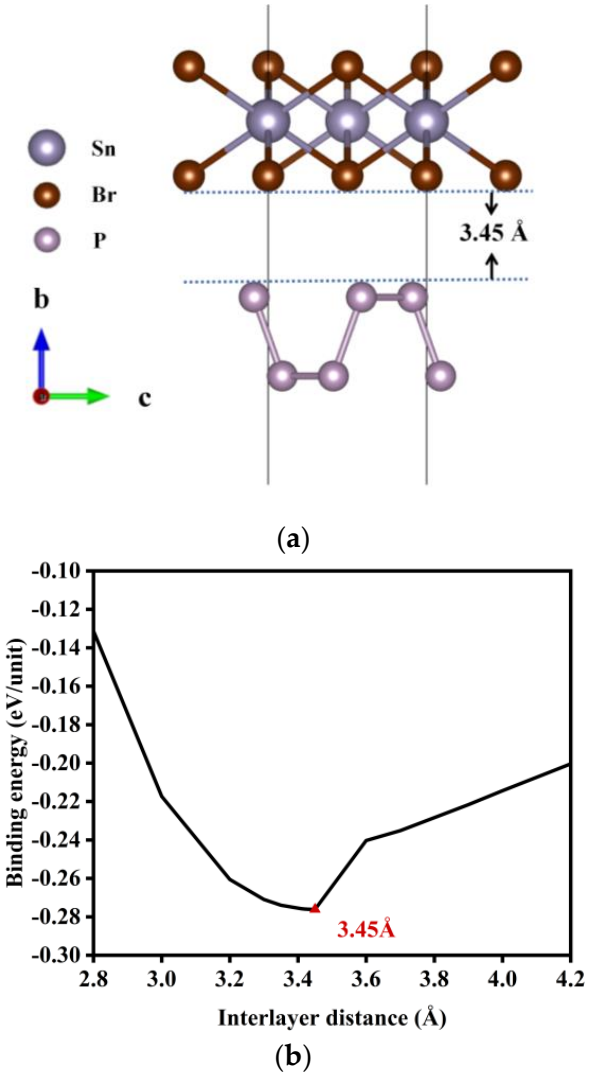

Figure 1. (**a**) The front view of P/$SnBr_2$ heterojunction; (**b**) curve of system energy changing with layer spacing.

In order to determine the most stable interlayer distance of the heterojunction, we calculated the binding energy, which was given by:

$$E_b = \left(E_{P/SnBr_2} - E_P - E_{SnBr_2}\right)/n$$

where $E_{P/SnBr_2}$, E_P and E_{SnBr_2} represent the total energy of the heterojunction, phosphorene and $SnBr_2$ monolayer, respectively. n indicates the number of P in the unit cell in the heterojunction, and a smaller binding energy indicates a more stable material structure. To ensure that the $P/SnBr_2$ heterojunction had the lowest binding energy, we gradually increased the layer spacing from 2.8 Å to 4.2 Å and calculated their corresponding binding energies separately to obtain the relationship between the binding energy and the layer spacing, as shown in Figure 1b. It can be seen from Figure 1b that the binding energy of the heterojunction system was the lowest at the layer spacing of 3.45 Å. Therefore, the layer spacing was taken as 3.45 Å when the structure was constructed, and this layer spacing was used in the subsequent electronic characteristic analysis in this paper.

3.2. The Electronic Properties of $P/SnBr_2$ Heterojunctions

Based on the most stable heterojunction system, we further calculated the energy band structures of the phosphorene (shown in red) and $SnBr_2$ (shown in blue) monolayers and the projected energy band structures of the heterojunctions, as shown in Figure 2a–c, respectively.

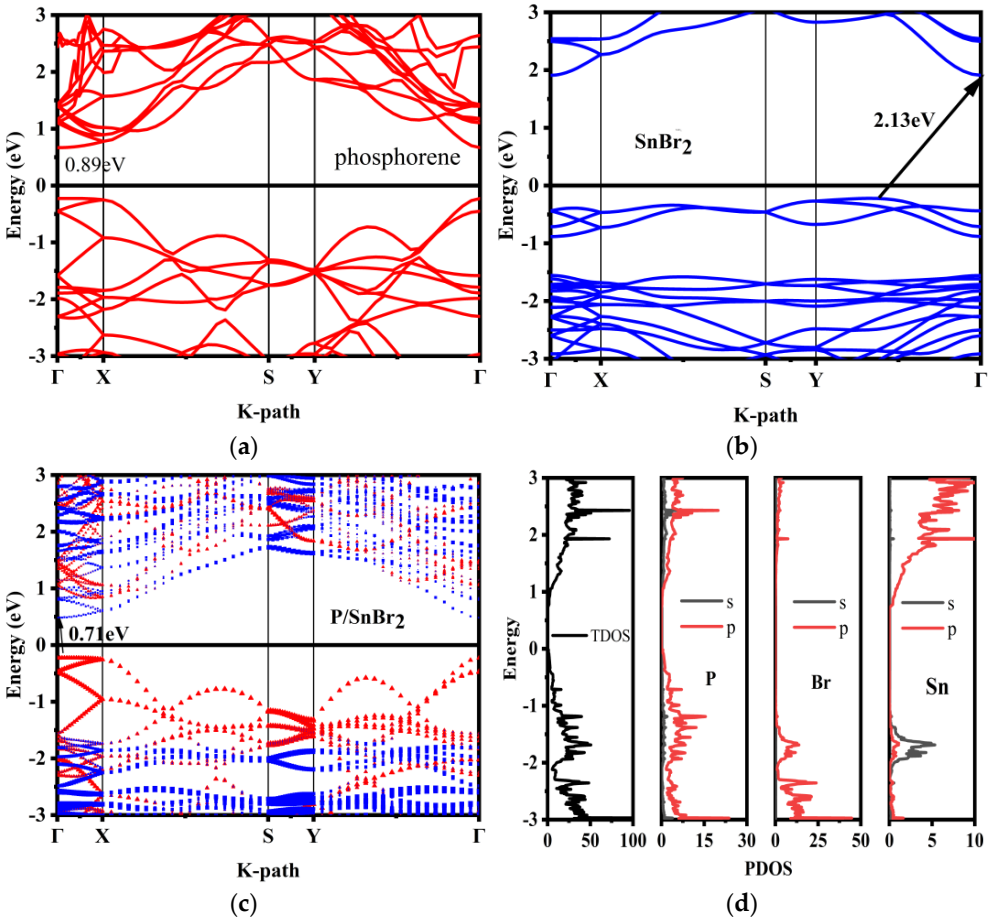

Figure 2. (**a**) Band structures of phosphorene; (**b**) band structures of $SnBr_2$; (**c**) projected band structures of the $P/SnBr_2$; (**d**) state density diagram of the heterojunction.

The monolayer phosphorene exhibited direct bandgap semiconductor properties at the high symmetry point gamma with a bandgap of 0.89 eV. The indirect bandgap of the $SnBr_2$ monolayer was 2.13 eV, with the conduction band minimum (CBM) occurring

at the gamma point and the valence band maximum (VBM) located between the high symmetry point Y and the gamma point. The P/$SnBr_2$ heterojunction was an indirect bandgap semiconductor with a bandgap of 0.71 eV. In the projected energy band structure of the heterojunction, the red triangle represents the part contributed by phosphorene and the blue square represents the part contributed by $SnBr_2$. It can be seen that its CBM and VBM were located on $SnBr_2$ and phosphorus, respectively. VBM was mainly contributed by phosphorene, while CBM was mainly contributed by a mixture of $SnBr_2$ and a small amount of phosphorene. The total density of states (TDOSs) and partial density of state (PDOS) of the heterojunction system are shown in Figure 2d. It can be observed that the VBM of the P/$SnBr_2$ heterojunction primarily stemmed from the 2s and 2p orbitals of the P atom, whereas the CBM originated from the 5p orbitals of the Sn atom in $SnBr_2$, along with the 2p orbitals of the P atom.

In order to fully understand the electronic structure properties of the P/$SnBr_2$ heterostructure, we performed partial charge density calculations and analysis for the CBM and VBM, as shown in Figure 3a. It can be clearly seen that the VBM came from phosphorene, and the CBM mainly came from $SnBr_2$, with some coming from phosphorene, which is consistent with the conclusion of the energy band structure diagram of the heterojunction.

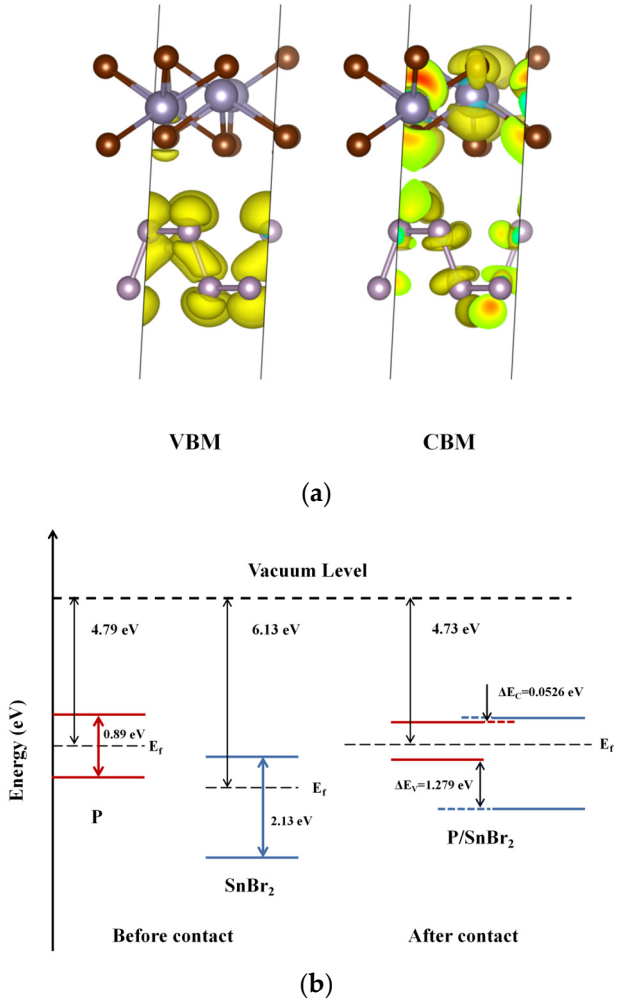

Figure 3. (**a**) The real-space charge densities of the VBM and CBMfor P/$SnBr_2$; (**b**) the energy band alignment of the P/$SnBr_2$ heterojunction.

We also calculated the energy band shifts of the P/$SnBr_2$ heterojunction by using the vacuum energy level as a standard reference point for the different systems. The VBM and CBM band energy alignments were plotted in Figure 3b. It was found that the energy band edges of phosphorene and $SnBr_2$ monolayer were (−0.228, 0.525) eV and

(−1.507, 0.577) eV, respectively, based on our calculations. This indicated that the CBM of phosphorene was close to that of $SnBr_2$, while its VBM was higher than that of $SnBr_2$. In addition, we also calculated the conduction band and valence band shifts after the contact of isolated single molecular layers using the core-level alignment method. After constructing the heterojunction system, the energy differences between the VBM and CBM of the two monolayers were 0.0526 eV and 1.279 eV, respectively. This conclusion was consistent with the previous projected energy band diagram of the $P/SnBr_2$ heterojunction, which further indicated the type I band arrangement formed by the $P/SnBr_2$ heterojunction. The calculated work function of the $P/SnBr_2$ heterojunction was 4.73 eV. Our findings indicated that the Fermi energy level of the heterojunction was −0.02 eV. The variance in the energy band shift before and after contact was primarily due to the charge redistribution induced by the formation of the heterojunction. Type I heterojunctions have a unique band-edge arrangement that prevents electron–hole recombination and spontaneously separates free electrons and holes. It can be used in the field of optoelectronics and can achieve efficient photoelectron and solar energy conversion.

The average planar electrostatic potential of the $P/SnBr_2$ heterojunction, normal to the heterostructure (along the Z-direction), is illustrated in Figure 4a. The outcomes demonstrated that the potential of the phosphorene monolayer was more profound compared to that of the $SnBr_2$ monolayer. The heterojunction bilayer exhibited an electric potential difference of 13.18 eV, which implied the existence of an electrostatic field perpendicular to the interface direction. Moreover, due to the higher electron negativity of phosphorene compared to the $SnBr_2$ monolayer, the former has a more profound electrostatic potential compared to the latter. Therefore, when the $P/SnBr_2$ heterostructure was formed, electrons were spontaneously transferred from the $SnBr_2$ layer to the phosphorene layer, which generated a strong built-in electric field through the heterostructure. The inherent electric field generated in the heterostructure enhanced the segregation efficiency of the photogenerated charge carriers and reduced their recombination, leading to the development of a $P/SnBr_2$ heterostructure that exhibited excellent optoelectronic properties. In order to display the charge transfer of heterostructures more clearly, we calculated the average electron density difference in the heterostructures along the Z-direction. As shown in Figure 4b, the yellow part represented the aggregation of electrons and the cyan part represented the dissipation of electrons; the positive values represented the gain of electrons and the negative values represented the loss of electrons. We can see that after the formation of the heterojunction, the charges of the two layers were redistributed, with the phosphorene layer losing electrons and the $SnBr_2$ monolayer gaining electrons. In order to quantitatively estimate the electron transfer, we performed a Bader charge analysis. The amount of charge transferred from the phosphorene monolayer to $SnBr_2$ monolayer was 0.149 e.

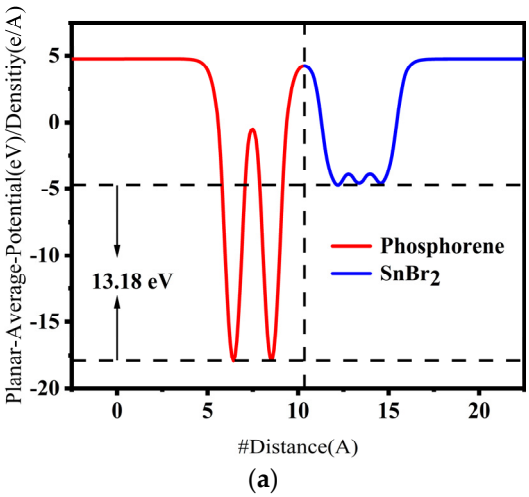

(**a**)

Figure 4. *Cont.*

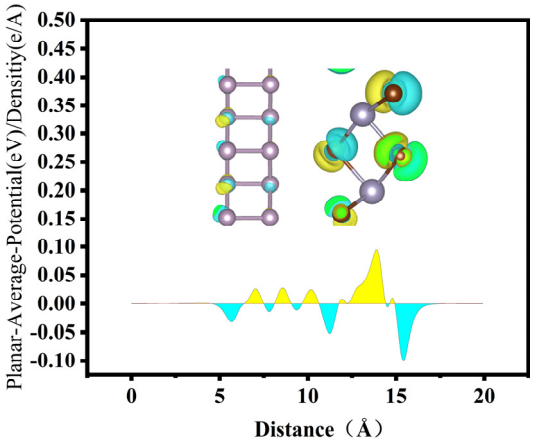

(**b**)

Figure 4. (**a**) Average electrostatic potential distribution of $P/SnBr_2$ heterojunction in the z-direction; (**b**) differential electron density of $P/SnBr_2$ along the Z direction.

3.3. The Regulation of the Electronic Structure Properties of P/SnBr$_2$ Heterojunctions by Electric Fields

The application of external electric fields has been shown to be an effective strategy for regulating the electronic structure of heterojunctions [43]. Thus, we conducted a systematic investigation of the impact of the vertical electric fields on the energy band structure of the $P/SnBr_2$ heterojunction. The positive direction of the electric field was designated as the direction from the phosphorene layer to the $SnBr_2$ layer along the Z-axis. Figure 5a shows the interaction between the $P/SnBr_2$ heterojunction and the external vertical electric field. Here, the applied vertical electric field ranged from -0.8/Å to 0.8 V/Å. With the increase in the positive electric field, the bandgap of the heterojunction gradually decreased, while with the increase in the negative electric field, the bandgap correspondingly increased. It showed that the bandgap of the heterojunction was positively related with the external electric field; the bandgap values varied between -0.08 and 0.82 eV. The heterojunction was metallic when the electric field was greater than 0.8 V/Å. When the electric field was less than -0.4 V/Å, the modulation of the bandgap by the electric field became insignificant and the electric field no longer played an important role in regulating the bandgap.

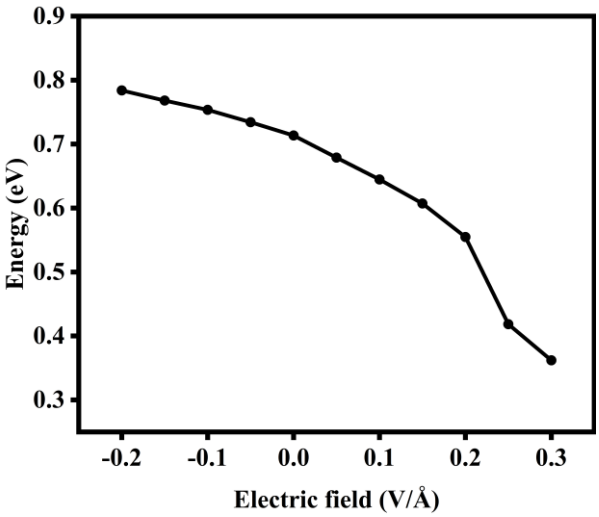

(**a**)

Figure 5. *Cont.*

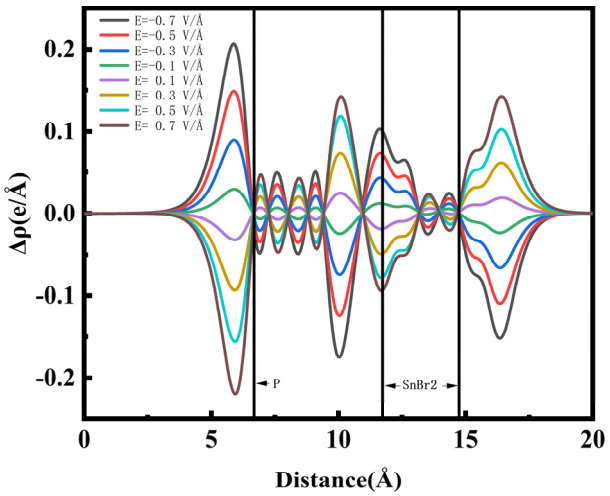

Figure 5. (**a**) the curve illustrating the change in bandgap for the P/$SnBr_2$ heterojunction under distinct electric fields; (**b**) the average charge density difference across the plane of the P/$SnBr_2$ heterostructure in the z-direction under diverse electric fields.

In order to better understand the effect of the electric field on the interfacial properties of the P/$SnBr_2$ heterostructures, we calculated the difference in the average planar charge density of the heterostructures along the vertical z-axis under different positive and negative electric fields. From Figure 5b, it can be clearly seen that the electron transfer increased rapidly when a negative electric field was applied, while the electron transfer from phosphorene to $SnBr_2$ increased gradually under a positive electric field as the electric field increased to 0.7 V/Å. Our findings demonstrated that the intensity and orientation of the electric field significantly influenced the electronic and interfacial properties of the P/$SnBr_2$ heterostructures. This effect could efficiently adjust the energy band structure and interfacial interactions, thereby, enhancing their potential applications in nanoscale optoelectronic devices.

3.4. Effect and Regulation of Biaxial Strain on P/$SnBr_2$ Heterojunctions

During the formation of heterostructures, strains are difficult to remove due to the influence of external forces or substrates. Meanwhile, mechanical strain has been proved to be an effective method for regulating the electronic properties in 2D applications [44,45]. Therefore, we studied the electronic properties of the P/$SnBr_2$ heterosjunctions under the biaxial strain conditions of −8%~8%.

To simulate the mechanical strain, we modified the lattice constants along the x- and y-directions, followed by a full optimization of atomic positions based on these changes. The strain was defined as $\varepsilon = (L-L_0)/L_0$, wherein L and L_0 were the values of the lattice constants in the strained and original states, respectively. The positive and negative values of strain applied to the P/$SnBr_2$ heterojunction ($\varepsilon > 0$) indicated the tensile and compressive strains applied to the system, respectively. We changed the biaxial strain applied on the P/$SnBr_2$ heterojunction from −8% to +8%, with a step of 2%. The evolution of the energy band structure of the P/$SnBr_2$ heterojunction is shown in Figure 6. The projected energy band diagrams for applying −8%, −6%, 4% and 6% strains are shown in Figure 7a–d, respectively.

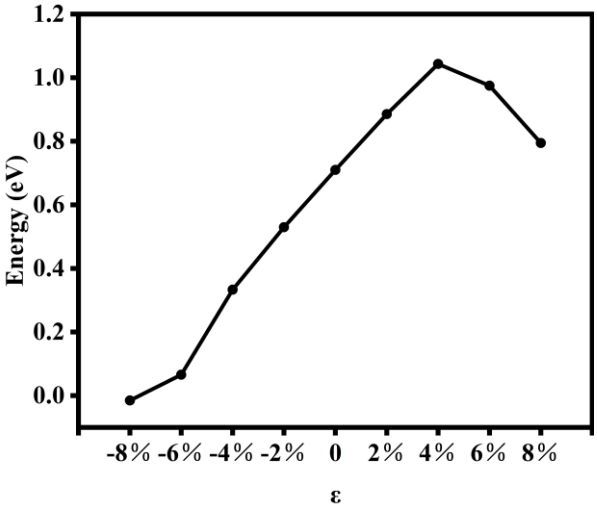

Figure 6. The curve depicts the alteration of the bandgap for the P/$SnBr_2$ heterojunction under biaxial strains.

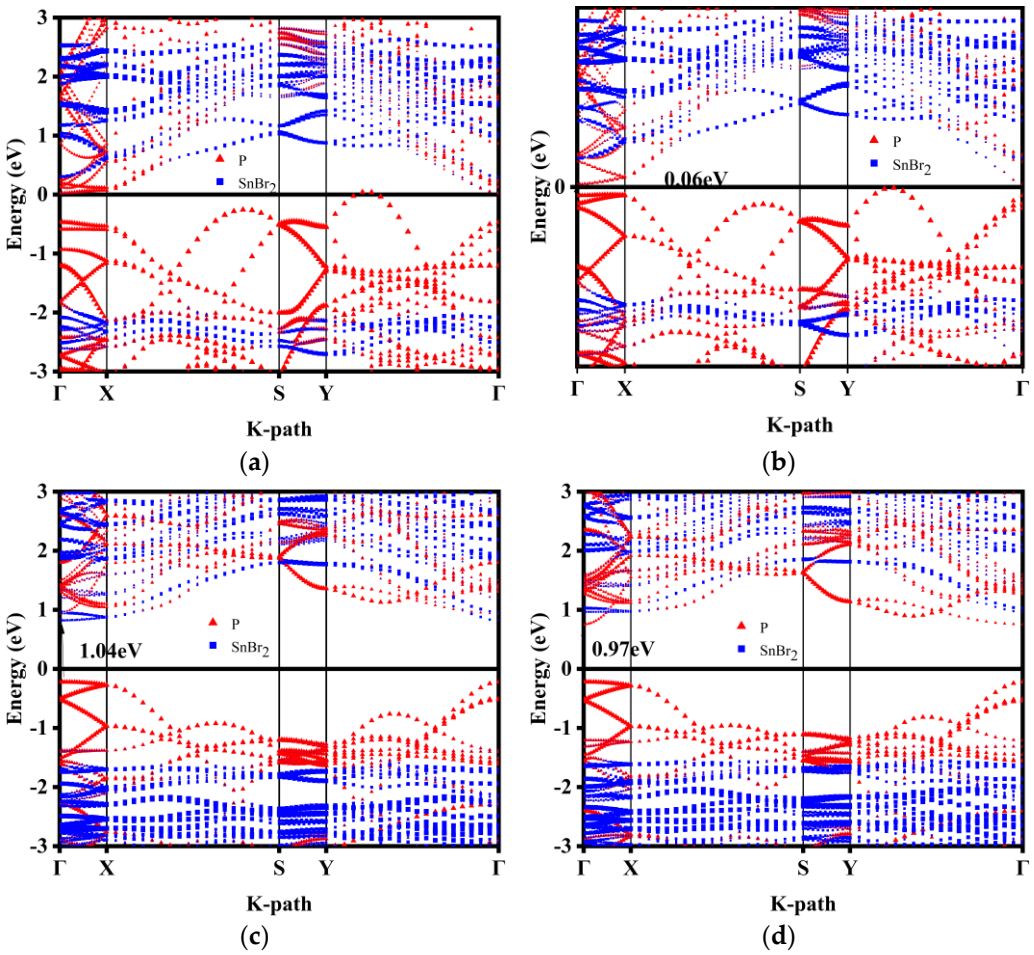

Figure 7. Projected band structure diagrams of the heterojunction at a −8% strain (**a**), at a −6% strain (**b**), at a 4% strain (**c**) and at a 6% strain (**d**).

Figures 6 and 7 show that the bandgap of the P/$SnBr_2$ heterojunction decreased from 0.71 eV to 0.53 eV (when the strain was −2%) under the effect of compressive strain. With the further increase in compressive strain, when the strain was −6%, the CBM value was gradually lower than the VBM value, and the bandgap of the heterojunction was 0.06 eV. When the strain was −8%, the value of the CBM was lower than that of the VBM. Since the

CBM and VBM come from P and $SnBr_2$, respectively, the energy band arrangement of the heterojunction underwent a type I to type III transition when the strain was less than −8%. Then, the bandgap of the heterojunction was closed and the system appeared metallic.

Under the tensile strain, the CBM shifted slightly upward and the VBM shifted slightly downward when the tensile strain increased to 2%, resulting in an increase in the bandgap of the $P/SnBr_2$ heterojunction from 0.71 eV to 0.89 eV. With the tensile strain increased to 4%, the bandgap of the $P/SnBr_2$ heterojunction reached a maximum of 1.04 eV. After that, with the increase in the tensile strain, the bandgap of the heterojunction decreased gradually, but the value of the bandgap was still greater than the initial bandgap without strain. Meanwhile, we observed that at 6% and 8% tensile strain, the VBM shifted from a position between Γ and X to the Γ point, leading to a transition in the $P/SnBr_2$ heterojunction from an indirect bandgap to a direct bandgap.

It can be inferred that the application of biaxial strains is an effective means to regulate the energy bandgap and energy band alignment of the heterostructures. There exists a range of linear regulation of biaxial strain on the bandgap of $P/SnBr_2$ heterojunctions; the strain range was −8%~4%, and the bandgap changed from metallicity to 1.04 eV. The transition from indirect to direct bandgap could be achieved at 6% and 8% strains.

4. Conclusions

In summary, the paper presented a systematic study of heterojunctions composed of phosphorene and $SnBr_2$ using the DFT method. We found that the external electric field and biaxial strain could effectively regulate the electronic properties of the $P/SnBr_2$ heterojunctions. In a certain range of electric field and strain regulation, the bandgap changed linearly. When the biaxial strain increased to −8% or the electric field strength was greater than 0.8 V/Å, the heterojunction became a metallic system. When the compression strain was greater than 8%, the band alignment shifted from type I to type III. An indirect to direct band gap transition occurred when the tensile strain was greater than 6%. The energy band alignment of the heterojunction was type I. Such structures allows the separation of electrons and holes in real space. Thus, the recombination of carriers is reduced, which is very beneficial to the application of materials in solar cells. The results of the paper could provide certain valuable parameters and guidance for the research and related experiments in the application of $SnBr_2$-based heterojunctions for the manufacture of solar cells and optoelectronic devices.

Author Contributions: Conceptualization, K.Y. and Z.D.; methodology, K.Y. and Z.D.; software, K.Y. and Z.D.; validation, K.Y. and Z.D.; formal analysis, K.Y., J.S. and Z.D.; investigation, K.Y., Z.D. and Q.H.; resources, K.Y. and Z.D.; data curation, K.Y. and Z.D.; writing—original draft preparation, K.Y. and Z.D.; writing—review and editing, K.Y. and Z.D.; visualization, K.Y. and Z.D.; supervision, K.Y. and Z.D.; project administration, K.Y., Q.L. and Z.D.; funding acquisition, Z.D., J.S. and Q.L. All authors have read and agreed to the published version of the manuscript.

Funding: This work was supported by the Key Project of the Foundation of Anhui Education Committee, China (2022AH050066, KJ2019A0020), the National Natural Science Foundation of China (21773001), Anhui Project (Z010118169), the Natural Science Foundation of Anhui Province (2108085MA16).

Data Availability Statement: Not applicable.

Acknowledgments: Computational resources from the Shanghai Supercomputer Center and Hefei Advanced Computing Center are acknowledged.

Conflicts of Interest: The authors declare no conflict of interest.

References

1. Geim, A.K.; Novoselov, K.S. The rise of graphene. *Nat. Mater.* **2007**, *6*, 183–191. [CrossRef]
2. Novoselov, K.S.; Geim, A.K.; Morozov, S.V.; Jiang, D.; Zhang, Y.; Dubonos, S.V.; Grigorieva, I.V.; Firsov, A.A. Electric field effect in atomically thin carbon films. *Science* **2004**, *306*, 666–669. [CrossRef] [PubMed]
3. Yang, R.; Fan, J.; Sun, M. Transition metal dichalcogenides (TMDCs) heterostructures: Optoelectric properties. *Front. Phys.* **2022**, *17*, 43202. [CrossRef]
4. Cianci, S.; Blundo, E.; Felici, M.; Polimeni, A.; Pettinari, G. Tailoring the optical properties of 2D transition metal dichalcogenides by strain. *Opt. Mater.* **2022**, *125*, 112087. [CrossRef]
5. Ashhadi, M.; Hadavi, M.S.; Sarri, Z. Electronic transport properties and first-principles study of graphene/h-BN and h-BN bilayers. *Phys. E Low Dimens. Syst. Nanostruct.* **2017**, *87*, 312–316. [CrossRef]
6. Brent, J.R.; Savjani, N.; Lewis, E.A.; Haigh, S.J.; Lewis, D.J.; O'Brien, P. Production of few-layer phosphorene by liquid exfoliation of black phosphorus. *Chem. Commun.* **2014**, *50*, 13338–13341. [CrossRef]
7. Carvalho, A.; Wang, M.; Zhu, X.; Rodin, A.S.; Su, H.; Neto, A.H.C. Phosphorene: From theory to applications. *Nat. Rev. Mater.* **2016**, *1*, 16061. [CrossRef]
8. Novoselov, K.S.; Mishchenko, A.; Carvalho, A.; Neto, A.H.C. 2D materials and van der Waals heterostructures. *Science* **2016**, *353*, aac9439. [CrossRef] [PubMed]
9. Chen, Y.; Wang, X.; Wu, G.; Wang, Z.; Fang, H.; Lin, T.; Sun, S.; Shen, H.; Hu, W.; Wang, J.; et al. High-performance photovoltaic detector based on $MoTe_2/MoS_2$ van der Waals heterostructure. *Small* **2018**, *14*, 1703293. [CrossRef]
10. Yang, Y.; Wang, Z. A two-dimensional MoS_2/C_3N broken-gap heterostructure, a first principles study. *RSC Adv.* **2019**, *9*, 19837–19843. [CrossRef]
11. Cui, X.; Troadec, C.; Wee, A.T.S.; Huang, Y.L. Surface nanostructure formation and atomic-scale templates for nanodevices. *ACS Omega* **2018**, *3*, 3285–3293. [CrossRef] [PubMed]
12. Zhao, K.; He, D.; Fu, S.; Bai, Z.; Miao, Q.; Huang, M.; Wang, Y.; Zhang, X. Interfacial Coupling and Modulation of van der Waals Heterostructures for Nanodevices. *Nanomaterials* **2022**, *12*, 3418. [CrossRef]
13. Zhang, J.L.; Han, C.; Hu, Z.; Wang, L.; Liu, L.; Wee, A.T.; Chen, W. 2D phosphorene: Epitaxial growth and interface engineering for electronic devices. *Adv. Mater.* **2018**, *30*, 1802207. [CrossRef] [PubMed]
14. Tapia, M.A.; Gusmão, R.; Serrano, N.; Sofer, Z.; Ariño, C.; Díaz-Cruz, J.M.; Esteban, M. Phosphorene and other layered pnictogens as a new source of 2D materials for electrochemical sensors. *TrAC Trends Anal. Chem.* **2021**, *139*, 116249. [CrossRef]
15. Zhang, W.; Li, F.; Hu, J.; Zhang, P.; Yin, J.; Tang, X.; Jiang, Y.; Wu, B.; Ding, Y. Strain engineering on transmission carriers of monolayer phosphorene. *J. Phys. Condens. Matter* **2017**, *29*, 465501. [CrossRef] [PubMed]
16. Yang, J.; Lu, Y. Optical properties of phosphorene. *Chin. Phys. B* **2017**, *26*, 034201. [CrossRef]
17. Liang, J.; Hu, Y.; Zhang, K.; Wang, Y.; Song, X.; Tao, A.; Liu, Y.; Jin, Z. 2D layered black arsenic-phosphorus materials: Synthesis, properties, and device applications. *Nano Res.* **2022**, *15*, 3737–3752. [CrossRef]
18. Jiang, Z.T.; Lv, Z.T.; Zhang, X.D. Electromechanical field effect transistors based on multilayer phosphorene nanoribbons. *Phys. Lett. A* **2017**, *381*, 1962–1966. [CrossRef]
19. Luo, Y.; Xie, Y.; Ye, X.; Wang, Y. A self-powered phosphorene photodetector with excellent spin-filtering and spin-valve effects. *Phys. Chem. Chem. Phys.* **2019**, *21*, 7613–7617. [CrossRef]
20. Li, J.; Guo, C.; Li, C.M. Recent Advances of Two-Dimensional (2D) MXenes and Phosphorene for High-Performance Rechargeable Batteries. *ChemSusChem* **2020**, *13*, 1047–1070. [CrossRef]
21. Hao, F.; Stoumpos, C.C.; Cao, D.H.; Chang, R.P.H.; Kanatzidis, M.G. Lead-free solid-state organic–inorganic halide perovskite solar cells. *Nat. Photonics* **2014**, *8*, 489–494. [CrossRef]
22. Fu, P.; Huang, M.; Shang, Y.; Yu, N.; Zhou, H.-L.; Zhang, Y.-B.; Chen, S.; Gong, J.; Ning, Z. Organic-Inorganic layered and hollow tin bromide perovskite with tunable broadband emission. *ACS Appl. Mater. Interfaces* **2018**, *10*, 34363–34369. [CrossRef] [PubMed]
23. Dorrell, W.; Pirie, H.; Gardezi, S.M.; Drucker, N.C.; Hoffman, J.E. van der Waals metamaterials. *Phys. Rev. B* **2020**, *101*, 121103. [CrossRef]
24. Wang, Q.; Zhang, L.; Liu, X.; Li, S. Two-Dimensional Semiconductor Heterojunctions for Optoelectronics and Electronics. *Front. Energy Res.* **2021**, *9*, 802055. [CrossRef]
25. Di Bartolomeo, A. Emerging 2D materials and their van der Waals heterostructures. *Nanomaterials* **2020**, *3*, 579–588. [CrossRef]
26. Song, D.Y.; Chu, D.; Lee, S.K.; Pak, S.W.; Kim, E.K. High photoresponsivity from multilayer MoS_2/Si heterojunction diodes formed by vertically stacking. *J. Appl. Phys.* **2017**, *122*, 124505. [CrossRef]
27. Zhu, W.; Xue, Z.; Wang, G.; Zhao, M.; Chen, D.; Guo, Q.; Liu, Z.; Feng, X.; Ding, G.; Chu, P.K.; et al. Graphene quantum dot-decorated vertically oriented graphene/germanium heterojunctions for near-infrared photodetectors. *ACS Appl. Nano Mater.* **2020**, *3*, 6915–6924. [CrossRef]
28. Zhou, J.; Kong, X.; Sekhar, M.C.; Lin, J.; Le Goualher, F.; Xu, R.; Wang, X.; Chen, Y.; Zhou, Y.; Zhu, C.; et al. Epitaxial synthesis of monolayer $PtSe_2$ single crystal on $MoSe_2$ with strong interlayer coupling. *ACS Nano* **2019**, *13*, 10929–10938. [CrossRef]
29. He, C.; Han, F.S.; Zhang, J.H.; Zhang, W.X. The In 2 SeS/gC_3N_4 heterostructure: A new two-dimensional material for photocatalytic water splitting. *J. Mater. Chem. C* **2020**, *8*, 6923–6930. [CrossRef]
30. Zhang, F.; Li, W.; Dai, X. Modulation of electronic structures of $MoSe_2/WSe_2$ van der Waals heterostructure by external electric field. *Solid State Commun.* **2017**, *266*, 11–15. [CrossRef]

31. Barhoumi, M.; Lazaar, K.; Said, M. Electronic and vibrational properties of TMDs heterogeneous bilayers, nontwisted bilayers silicene/TMDs heterostructures and photovoltaic heterojunctions of fullerenes with TMDs monolayers. *Phys. E Low Dimens. Syst. Nanostruct.* **2018**, *104*, 155–164. [CrossRef]
32. Cassabois, G.; Valvin, P.; Gil, B. Hexagonal boron nitride is an indirect bandgap semiconductor. *Nat. Photonics* **2016**, *10*, 262–266. [CrossRef]
33. Liu, H.; Neal, A.T.; Zhu, Z.; Luo, Z.; Xu, X.; Tomanek, D.; Ye, P.D. Phosphorene: An unexplored 2D semiconductor with a high hole mobility. *ACS Nano* **2014**, *8*, 4033–4041. [CrossRef] [PubMed]
34. Zhou, C.; Tian, Y.; Wang, M.; Rose, A.; Besara, T.; Doyle, N.K.; Yuan, Z.; Wang, J.C.; Clark, R.; Hu, Y.; et al. Low-dimensional organic tin bromide perovskites and their photoinduced structural transformation. *Angew. Chem. Int. Ed.* **2017**, *56*, 9018–9022. [CrossRef] [PubMed]
35. Xu, Y.; Jiang, K.-J.; Wang, P.; Gu, W.-M.; Yu, G.-H.; Zhou, X.; Song, Y. Highly oriented quasi-2D layered tin halide perovskites with 2-thiopheneethylammonium iodide for efficient and stable tin perovskite solar cells. *New J. Chem.* **2022**, *46*, 2259–2265. [CrossRef]
36. Kresse, G.; Furthmüller, J. Efficiency of ab-initio total energy calculations for metals and semiconductors using a plane-wave basis set. *Comput. Mater. Sci.* **1996**, *6*, 15–50. [CrossRef]
37. Kresse, G.; Hafner, J. Ab initio molecular dynamics for liquid metals. *Phys. Rev. B* **1993**, *47*, 558–561. [CrossRef]
38. Ma, Y.; Zhao, X.; Niu, M.; Dai, X.; Li, W.; Wang, X.; Zhao, M.; Wang, T.; Tang, Y. Modulation of interfacial electronic properties in PbI_2 and BN van der Waals heterobilayer via external electric field. *Appl. Surf. Sci.* **2017**, *411*, 46–52. [CrossRef]
39. Su, J.; Liu, H.; Jia, Z. Electric field tunable electronic properties of antimonene/graphyne van der Waals heterostructure. *J. Alloys Compd.* **2022**, *909*, 164653. [CrossRef]
40. Sharma, N.K.; Sahoo, S.; Sahu, M.C.; Mallik, S.K.; Jena, A.K.; Sharma, H.; Gupta, S.K.; Ahuja, R.; Sahoo, S. Electronic bandstructure modulation of MoX_2/ZnO (X: S, Se) heterostructure by applying external electric field. *Surf. Interfaces* **2022**, *29*, 101817. [CrossRef]
41. Monkhorst, H.J.; Pack, J.D. Special points for Brillouin-zone integrations. *Phys. Rev. B* **1976**, *13*, 5188–5192. [CrossRef]
42. Wei, Y.; Wang, F.; Zhang, W.; Zhang, X. The electric field modulation of electronic properties in a type-II phosphorene/PbI_2 van der Waals heterojunction. *Phys. Chem. Chem. Phys.* **2019**, *21*, 7765–7772. [CrossRef] [PubMed]
43. Baskoutas, S.; Paspalakis, E.; Terzis, A.F. Electronic structure and nonlinear optical rectification in a quantum dot: Effects of impurities and external electric field. *J. Phys. Condens. Matter* **2007**, *19*, 395024. [CrossRef]
44. Wang, Y.; Wang, B.; Huang, R.; Gao, B.; Kong, F.; Zhang, Q. First-principles study of transition-metal atoms adsorption on MoS_2 monolayer. *Phys. E Low Dimens. Syst. Nanostruct.* **2014**, *63*, 276–282. [CrossRef]
45. Li, X.H.; Wang, B.J.; Cai, X.L.; Zhang, L.W.; Wang, G.D.; Ke, S.H. Tunable electronic properties of arsenene/GaS van der Waals heterostructures. *RSC Adv.* **2017**, *7*, 28393–28398. [CrossRef]